Dependence of acoustic levitation capabilities on geometric parameters

W. J. Xie* and B. Wei
Department of Applied Physics, Northwestern Polytechnical University, Xi'an 710072, People's Republic of China
(Received 25 April 2002; published 28 August 2002)

A two-cylinder model incorporating boundary element method simulations is developed, which builds up the relationship between the levitation capabilities and the geometric parameters of a single-axis acoustic levitator with reference to wavelength. This model proves to be successful in predicting resonant modes of the acoustic field and explaining axial symmetry deviation of the levitated samples near the reflector and emitter. Concave reflecting surfaces of a spherical cap, a paraboloid, and a hyperboloid of revolution are investigated systematically with regard to the dependence of the levitation force on the section radius R_b and curvature radius R (or depth D) of the reflector. It is found that the levitation force can be remarkably enhanced by choosing an optimum value of R or D, and the possible degree of this enhancement for spherically curved reflectors is the largest. The degree of levitation force enhancement by this means can also be facilitated by enlarging R_b and employing a lower resonant mode. The deviation of the sample near the reflector is found likely to occur in case of smaller R_b, larger D, and a higher resonant mode. The calculated dependence of levitation force on R, R_b, and the resonant mode is also verified by experiment and finally demonstrated to be in good agreement with experimental results, in which considerably a strong levitation force is achieved to levitate an iridium sphere which has the largest density of 22.6 g/cm^3.

DOI: 10.1103/PhysRevE.66.026605 PACS number(s): 43.25.+y

I. INTRODUCTION

Containerless processing of materials eliminates the contamination from container walls and hence has significant applications in crucible-free solidification [1–4], noncontact measurement of physical properties of undercooled liquids [5–7], and investigation of fluid dynamics of free drops [8–10]. The containerless state of an object can be achieved by levitation techniques employing acoustic, aerodynamic, magnetic, electromagnetic, or electrostatic forces [10–17]. Among all these techniques, acoustic levitation has no special restriction on the levitated object such as its electric or magnetic properties, and no coupling with the strong heating effect such as that in electromagnetic levitation. Therefore, its application potential is as wide as to cover all the solids and liquids. Especially, it may find the most attractive applications in containerless processing of nonmetallic substances and metallic alloys with a low melting temperature.

The fundamental concept of acoustic levitation is the radiation force produced by sound, which was first recognized by Kundt in 1886 [18] and afterwards demonstrated by King [19] to be a nonlinear effect of small objects with a high intensity acoustic field. Here, the radius of the objects, R_S, should be smaller than the sound wavelength λ. It was shown that the force produced by a standing wave is much larger than that produce by a progressive wave, because the former is of the order of $(R_S/\lambda)^3$ whereas the latter is of the order of $(R_S/\lambda)^6$. Therefore, acoustic levitation generally utilizes standing waves. For example, in a plane standing wave, the magnitude of the radiation force varies sinusoidally in the vibration direction with a period of $\lambda/2$, which propels the small objects toward the pressure nodes (or velocity antinodes) in the absence of gravity. If the maximum of the acoustic radiation force is equal to or larger than the weight of an object, it is also possible to levitate that object free from rigid support in the gravitational field.

There are two elementary arrangements of an acoustic levitator [20]: triple axis and single axis. The single-axis levitator employs a sound emitter and a reflector facing each other, with the emitter-reflector axis parallel to the gravitational direction. Three emitter-reflector sets in an orthogonal arrangement combine into a triple-axis acoustic levitator. Obviously, the single-axis arrangement is more simple and convenient in addition to its great advantage of low cost.

During the last two decades, there was always a strong concern of the levitation force and levitation stability in the study of acoustic levitation [20–27], because the radiation force produced by sound or ultrasound is comparatively weak so that its applications are generally confined to light substances. Space environment [10,18] is a suggested means to facilitate the use of acoustic levitation, where the necessary restoring force to hold a sample is much small. But the opportunities for space experiment are fairly rare, hence more attention is paid to enhancing the levitation force and stability in terrestrial laboratories. Strong sonic/ultrasonic generators [22,23], carefully designed resonant chambers [18,20], different medium atmospheres with high pressures [24], and even arrays of multitransducers [25] have been taken as measures and given intensive investigations. It has also been recognized that reflectors and emitters with properly curved surfaces [21,23,25,26] will enhance the levitation force remarkably. In fact, reflectors with concave reflecting surface have been applied in a series of successful experiments on containerless processing of materials [23,27–30]. However, it is still unclear that in what way the levitation force/stability is dependent on the geometric parameters of the levitator.

Barmatz and Collas [18] developed a method to evaluate the levitation force and stability of levitated spheres in vari-

*Corresponding author. Email address: lmss@nwpu.edu.cn

ous acoustic fields. Their method was based on Gor'kov's theory [31], which gives the time-averaged potential for acoustic radiation force on a small rigid sphere in ideal fluids:

$$U=2\pi R_s^3[\langle p_{\rm in}^2\rangle/(3\rho_f c^2)-\rho_f\langle \mathbf{v}_{\rm in}^2\rangle/2], \tag{1}$$

where U is the time-averaged potential, $\langle p_{\rm in}^2\rangle$ and $\langle \mathbf{v}_{\rm in}^2\rangle$ are the mean square fluctuations of the incident pressure and velocity at the point where the sample with a radius of R_S is located, ρ_f and c are the density and sound speed of the fluid, respectively. Then the levitation positions were determined by finding the locations of potential minima that satisfy $\partial U/\partial x_i=0$, where x_i is the ith coordinate. The force components around such a potential minimum is characterized by the restoring force, which will draw back the sample when small random external forces push it slightly away from the equilibrium position. The components of this restoring force can be written as $F_i=-\kappa_i x_i$, where κ_i is the ith restoring force constant which can weigh the stability degree of a sample entrapped in the potential well. The acoustic radiation force components and restoring force constants can be described in terms of the time-averaged potential by

$$F_i=-\frac{\partial U}{\partial x_i} \tag{2}$$

and

$$\kappa_i=\frac{\partial^2 U}{\partial x_i^2}, \tag{3}$$

respectively. Barmatz and co-workers examined the acoustic potential in rectangular, cylindrical, and spherical resonant chambers, in which the incident acoustic fields had been known previously and written in analytical forms. However, for a practically used acoustic levitator, such as that with a concave reflector, the incident acoustic field is much more complicated, and it is proper to employ a numerical method [32].

In this paper, we propose a two-cylinder model for single-axis acoustic levitators. The incident acoustic field is obtained by solving the Helmholtz equation through the boundary element method. Then following Barmatz's approach, the levitation positions, the acoustic radiation force, and the restoring force constants are analyzed on the basis of the time-averaged potential, during which main attention is focused on the dependence of the levitation force and stability on geometric parameters of the reflector. In order to prove the reliability of this model, experimental results are also presented accordingly. The purpose of this paper is to shed light on the possibility and feasibility of improving an acoustic levitator's capabilities by optimizing its geometric parameters.

II. MODEL

Our model for single-axis acoustic levitator includes three parts: the sound emitter, the reflector, and the gas medium in which the former two are immersed, as shown in Fig. 1(a).

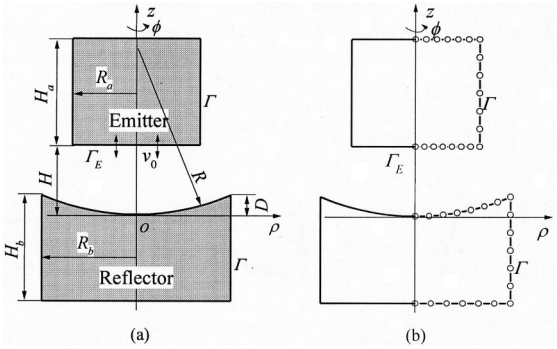

FIG. 1. Schematic of single-axis acoustic levitator. (a) Model, (b) division of the boundary elements.

The emitter is a cylinder with a length H_a and a section radius R_a. The reflector is also a cylinder with a length H_b, a section radius R_b, and its upper side cut out by a spherical surface with radius R ($R\geqslant R_b$). The vibrating cylinder and the reflector occupy the same axis of symmetry, namely, the z axis, which is in the antigravity direction. The bottom section of the upper cylinder acts as the emitting surface (denoted by Γ_E), which vibrates sinusoidally in the normal direction with an amplitude ν_0 and an angle frequency ω: $\nu=\nu_0\exp(-j\omega t)$. The other surfaces of the two cylinders are stationary. The interval H between the reflector and the vibrating surface is defined as the distance from the lowest point of the curved surface to the vibrating surface.

Based on this model, the incident acoustic field, described by velocity potential Φ will exist in an infinite space. But only the space between the reflector and the emitter, where the samples will be placed and levitated, is interesting for study. Because of the axial symmetry, Φ is not dependent on the circular coordinate ϕ and thus takes the form of $\Phi(\rho,z)\exp(-j\omega t)$. The spatial part $\Phi(\rho,z)$ satisfies the Helmholtz equation with boundary conditions

$$\nabla^2\Phi+k^2\Phi=0, \tag{4a}$$

$$\left.\frac{\partial\Phi}{\partial n}\right|_{\Gamma-\Gamma_E}=0, \tag{4b}$$

$$\left.\frac{\partial\Phi}{\partial n}\right|_{\Gamma_E}=-\nu_0, \tag{4c}$$

where k is the wave number, Γ is the surface of the cylinders with unit outward norm n, and Γ_E is the vibrating surface. The Helmholtz equation can be further written as the boundary integral equation over the surfaces of the two cylinders and then numerically solved by the boundary element method:

$$C(M)\Phi(M)=\int_\Gamma\left[\frac{\partial\Phi(Q)}{\partial n}\frac{\exp(jkr)}{4\pi r}-\Phi(Q)\frac{\partial}{\partial n}\left(\frac{\exp(jkr)}{4\pi r}\right)\right]d\Gamma(Q), \tag{5}$$

where M is an arbitrary point in space, Q is an arbitrary point at the surface Γ, r is the distance between M and Q, and C is a constant related to the geometric property at point M. The value of $4\pi C(M)$ is equal to the solid angle enclosed by the surface Γ at point M.

To get the numerical solution of Eq. (5), the boundary is divided into N elements with $N+2$ nodes as shown in Fig. 1(b). The values of $\Phi(\rho,z)$ are interpolated linearly between the corresponding every two adjacent nodes so that Eq. (5) can be transformed into an algebraic equation with the values of Φ at the nodes to be solved. When the values of Φ on the boundary are known, it is convenient to obtain the value at an arbitrary point in the field from Eq. (5). Then the incident pressure p_{in} and velocity $\boldsymbol{\nu}_{\mathrm{in}}$ of the incident acoustic field can be derived by the differentiation of Φ with respect to time and space, respectively.

For the purpose of simplicity, both the formulas and computation are nondimensionalized. The dimensionless length, velocity, sound pressure, and time-averaged potential are

$$\tilde{x}=kx, \tag{6}$$

$$\tilde{\boldsymbol{\nu}}=\boldsymbol{\nu}/\nu_0, \tag{7}$$

$$\tilde{p}/(\rho_f c\nu_0), \tag{8}$$

and

$$\tilde{U}=U/(2\pi R_s^3\rho_f\nu_0^2), \tag{9}$$

respectively. Then the dimensionless force components and restoring force constants take the forms $\tilde{F}_i=F_i/(2\pi R_s^3\rho_f\nu_0^2k)$ and $\tilde{\kappa}_i=\kappa_i/(2\pi R_s^3\rho_f\nu_0^2k^2)$, respectively. It should be noticed that our definition is slightly different from Barmatz's [18]: In our definition, ν_0 is the vibration amplitude of the emitter, whereas it denotes the maximum particle velocity in Barmatz's. The advantage of our definition is that it relates the sound source with the resultant acoustic field as well as with levitation capabilities. Additionally, the form of $\tilde{U}$ differs from Barmatz's by a factor of $\frac{1}{2}$.

By defining the dimensionless form of the velocity potential as $\tilde{\Phi}=k\Phi/\nu_0$, Eq. (5) can be transformed into

$$C(M)\tilde{\Phi}(M)=-\int_{\Gamma_E}\frac{\exp(j\tilde{r})}{4\pi\tilde{r}}d\tilde{\Gamma}(Q) -\int_{\Gamma}\tilde{\Phi}(Q)\frac{\partial}{\partial\tilde{n}}\left(\frac{\exp(j\tilde{r})}{4\pi\tilde{r}}\right)d\tilde{\Gamma}(Q), \tag{10}$$

where a quantity having a symbol $\sim$ on its top represents the corresponding dimensionless form of that quantity. A significant characteristic of Eq. (10) is that the solution of $\tilde{\Phi}(Q)$ on the boundary is only dependent on the dimensionless parameters $\tilde{R}_a$, $\tilde{R}_b$, $\tilde{R}$, $\tilde{H}_a$, $\tilde{H}_b$, and $\tilde{H}$, i.e., the geometric parameters of the levitator with reference to wavelength λ. This characteristic can be expressed as $\tilde{\Phi}=\tilde{\Phi}(Q,\{X_i\}/\lambda)$, where $\{X_i\}$ represents the set of R_a, R_b, R, H_a, H_b, and H. As a result, the subsequently derived quantities of $\tilde{U}$, $\tilde{F}_i$, and $\tilde{\kappa}_i$ take forms similar to forms as that of $\tilde{\Phi}$. In this way, a factor involving the geometric parameters of a single-axis acoustic levitator is ultimately introduced into the expressions of U, F_i, and κ_i, which weigh the capabilities of that levitator:

$$U=2\pi\rho_f\nu_0^2R_S^3\tilde{U}\left(Q,\frac{\{X_i\}}{\lambda}\right), \tag{11}$$

$$F_i=2\pi\rho_f k\nu_0^2R_S^3\tilde{F}_i\left(Q,\frac{\{X_i\}}{\lambda}\right), \tag{12}$$

$$\kappa_i=2\pi\rho_f k^2\nu_0^3R_S^3\tilde{\kappa}_i\left(Q,\frac{\{X_i\}}{\lambda}\right). \tag{13}$$

In order to extend the spherical reflecting surface to other surfaces of revolution, such as a paraboloid of revolution and a hyperboloid of revolution, another parameter D ($D\leqslant R_b$) is also defined in Fig. 1(a), which is the depth of the concave surface. We choose these three types of reflecting surfaces because their geometric shapes are simple. Giving D and R_b, the equations to describe them are definitely determined by $2Dz=D^2+R_b^2-\sqrt{D^2+R_b^2-4D^2\rho^2}$ for a spherical cap, $z/D=\rho^2/R_b^2$ for a paraboloid of revolution, and $2Dz=\sqrt{R_b^3-D^2-\rho^2}+D^2-R_b^2$ for a hyperboloid of revolution.

In principle, the emitter surface can also be extended to concave shapes. Nevertheless, for a practical single-axis acoustic levitator, the shape and size of the emitter have to meet the requirement of matching with the transducer, which narrows the choice of emitter shape and size. In contrast, it is free and easy to alter the reflector with various geometric parameters. Therefore, the effects of the reflector geometry on the levitation capabilities will be mainly discussed in this paper.

It has been recognized in experiment that the length of the reflector does not affect the levitation capabilities visibly. This seems reasonable since the acoustic field of interest is confined between the reflector and emitter. In the following sections, we will demonstrate that the roles of H_a and H_b are negligible in the geometric dependence of the levitation capabilities. Then, the geometrical parameters to be discussed are narrowed down to R_b, R, and H.

The single-axis acoustic levitation generally works at resonant states of the acoustic field, in which the distance between the reflector and the emitter is adjusted to some fixed values, namely, $H=H_1,H_2,H_3,\ldots$ ($H_1<H_2<H_3<\cdots$). For example, if the acoustic field between the reflector and emitter is simply regarded as a plane standing wave [19], H will satisfy $H_m=m\lambda/2$ ($m=1,2,3,...$). This means that the parameter H is not so arbitrarily chosen as the other parameters. In fact, the value H_m is dependent on the geometric parameters of the reflector and emitter. In the following analysis, it is more convenient to use the resonant mode number, symbolized by $H_1,H_2,H_3,\ldots$, rather than the actual values of H.

The behavior of $\tilde{U}$, $\tilde{F}_i$, and $\tilde{\kappa}_i$ as a function of $\{R/\lambda,R_b/\lambda,H_m/\lambda\}$ will be the main concerns of the following sections of this paper.

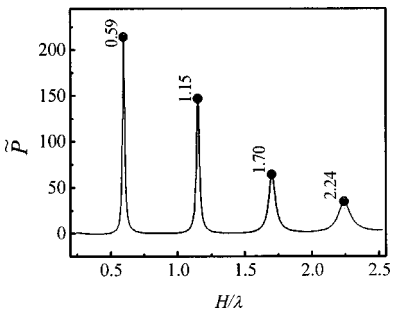

FIG. 2. The first four resonant modes calculated with $\tilde{R}_a = 3.858$, $\tilde{R}_b = 6.172$, and $\tilde{R} = 12.244$.

III. COMPUTATION PROCEDURES

We present a levitator with parameters $R_a = 12.5$ mm, $H_a = 15$ mm, $R_b = 20$ mm, $H_b = 20$ mm, $R = 40$ mm as a typical example to show the computation procedures. The physical conditions for the calculation are a transducer with a frequency of 16.7 kHz and a gas medium (air at room temperature and unit atmosphere pressure), which yields a wavelength of $\lambda = 20.36$ mm. This example actually represents a class of levitators with parameters $R_a = 0.614\lambda$, $H_a = 0.737\lambda$, $R_b = 0.982\lambda$, $H_b = 0.982\lambda$, $R = 1.965\lambda$.

The computation can be divided into three steps. At first, the resonant states are determined, which gives the values of H_m. In the second step, the incident acoustic field denoted by velocity potential Φ is calculated for a given resonant mode, from which the incident sound pressure and particle velocity, and ultimately, the time-averaged potential U can be derived. Based on the distribution of U with respect to space, the positions of the levitated sample, the maximum restoring force, and the restoring force constants around a potential well are determined at last.

A. Resonant modes of acoustic field

The resonant states are determined by studying the profile of acoustic radiation power P versus H, which in fact simulates the real experimental manipulation of finding the resonant states. The radiation power is calculated by

$$P = -\int_{\Gamma_E} \langle p \cdot \nu_n \rangle d\Gamma, \tag{14}$$

where $\langle\ \rangle$ denotes the time average over a period of the acoustic vibration. The dimensionless form of P is

$$\tilde{P} = Pk^2/(\rho_f c \nu_0^2). \tag{15}$$

Figure 2 shows a typical profile of the acoustic radiation power $\tilde{P}$ versus the reflector-emitter interval $\tilde{H}$ in dimensionless forms. There are four peaks in the profile and each of them denotes a resonant mode. The intensity and position of the peaks are dependent on $\tilde{R}_a$, $\tilde{R}_b$, and $\tilde{R}$ strongly but with negligible dependence on $\tilde{H}_a$ and $\tilde{H}_b$. To compare with the experiment that is conducted in air at room temperature ($c = 340$ m/s, $k = 0.309\ \mathrm{mm}^{-1}$, and $\lambda = 20.36$ mm), the applied values of $\tilde{R}_a$, $\tilde{R}_b$, and $\tilde{R}$ in Fig. 2 are taken to be the same as those in the experiment. It is easy to deduce the calculated resonant intervals of H_1, H_2, H_3, and H_4 to be 12.1, 23.4, 34.6, and 45.6 mm, which are in good agreement with the measured values of 11.9, 22.7, 34.1, and 45.3 mm. So our model is successful in predicting the resonant modes of the acoustic field.

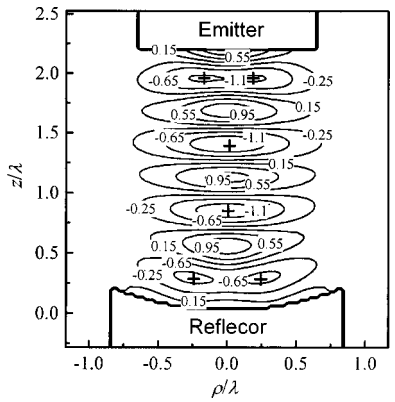

FIG. 3. Contour of $\tilde{U}$ in z-ρ plane with $\tilde{R}_a = 3.858$, $\tilde{R}_b = 5.092$, and $\tilde{R} = 12.244$. The symbol + denotes potential minimum.

The plane standing wave was usually employed in most of the previous theoretical analyses in which the resonant states satisfy $H_m = m\lambda/2$ ($m = 1,2,3,...$). Similarly, the resonant conditions in Fig. 2 can be written as $H_1 = 1.19\lambda/2$, $H_2 = 2.30\lambda/2$, $H_3 = 3.40\lambda/2$, and $H_4 = 4.48\lambda/2$. It can be seen that for a practically applied single-axis acoustic levitator, the resonant intervals between the reflector and emitter are a little larger than an integer times half a wavelength.

B. Time-averaged potential

For a given resonant mode, the time-averaged potential can be derived by Eq. (1) in a dimensionless form

$$\tilde{U} = \langle \tilde{p}_{\mathrm{in}}^2 \rangle/3 - \langle \tilde{\boldsymbol{\nu}}_{\mathrm{in}}^2 \rangle/2, \tag{16}$$

where $\tilde{p}_{\mathrm{in}} = -j\tilde{\Phi}$ and $\tilde{\boldsymbol{\nu}}_{\mathrm{in}} = -\mathrm{grad}\,\tilde{\Phi}$. The distribution of $\tilde{U}$ corresponding to mode H_4 in Fig. 2 is plotted in the z-ρ

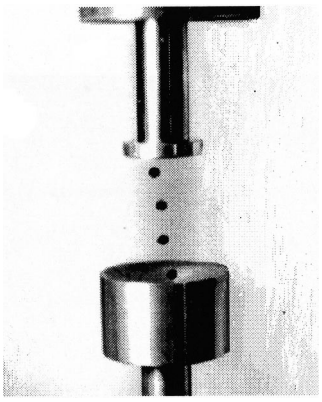

FIG. 4. Single-axis acoustic levitation of four polymer spheres with a diameter of 3 mm in air.

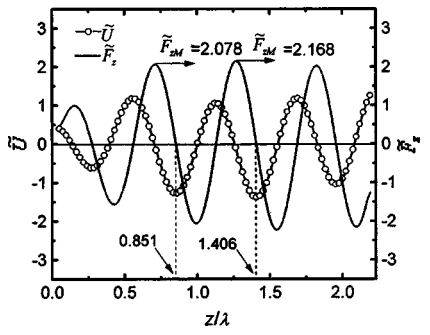

FIG. 5. Distribution of $\tilde{U}$ and $\tilde{F}_z$ along z axis ($\rho=0$).

plane, as shown in Fig. 3. The contour of $\tilde{U}$ has four potential minima. Each of them denotes an expected position for the levitated sample. The two minima near the reflector and the vibrating surface are cycles around the z axis and the other two are points at the z axis. The circle-shaped potential wells can explain the phenomenon that the samples near the reflector and the transducer head deviate from the cylindrical axis, such as that in Ref. [24] and our experiment as shown in Fig. 4. Figure 3 also shows that the vertical positions of the four potential wells are close to those predicted by plane standing wave approximation, which is $z=\lambda/4$, $3\lambda/4$, $5\lambda/4$, and $7\lambda/4$, respectively.

C. Restoring force and restoring force constants

The axial distribution of $\tilde{U}$ corresponding to Fig. 4 along the z axis is shown in Fig. 5. The z component of the dimensionless acoustic radiation force $\tilde{F}_z$ derived by $\tilde{F}_z=-\partial\tilde{U}/\partial\tilde{z}$ is also shown. It can be seen that closely below a potential well, there is a maximum of $\tilde{F}_z$, which determines the maximum levitation force of that potential well. This maximum value of $\tilde{F}_z$ is denoted by $\tilde{F}_{zM}$, as shown in Fig. 5. Therefore, the largest levitation force of a potential well is

$$F_{zM}=2\pi\rho_f k\nu_0^2 R_S^3 \tilde{F}_{zM}\left(Q,\frac{\{X_i\}}{\lambda}\right), \tag{17}$$

where Q is the position of that potential well. Since the potential wells with a vertical position of $z=0.851\lambda$ and 1.406λ are located at the z axis, the values of $\tilde{F}_{zM}$ for them are directly obtained to be 2.078 and 2.168. As to the other two off-axis potential wells, their radial positions should be found first, then the value of $\tilde{F}_{zM}$ for each of them can be obtained by the derivation of $\tilde{U}$ along a vertical line that goes through the potential minimum.

The distributions of $\tilde{U}$ and $\tilde{F}_\rho$ in horizontal planes are shown in Figs. 6(a) and 6(b), where $\tilde{F}_\rho$ is the ρ component of the dimensionless acoustic radiation force, derived by $\tilde{F}_\rho=-\partial\tilde{U}/\partial\tilde{\rho}$. Figures 6(a) and 6(b) represent the point-shaped and circle-shaped potential well, respectively, and the maximum restoring force to draw back the sample in horizontal directions is defined as $\tilde{F}_{\rho M}$ accordingly. To calculate the value of $\tilde{F}_{\rho M}$, the vertical position of the potential well should be found first, then the same procedure as for the derivation of $\tilde{U}$ along a horizontal line going through that potential minimum is followed.

Similarly, the restoring force constants, $\tilde{\kappa}_z$ and $\tilde{\kappa}_\rho$, can be obtained by the second derivation of $\tilde{U}$ with respect to $\tilde{z}$ and $\tilde{\rho}$, respectively, at the point where a potential minimum is located.

D. Influence of $\tilde{H}_a$ and $\tilde{H}_b$

Among the six geometric parameters, it has been found that the length of the cylinders, $\tilde{H}_a$ and $\tilde{H}_b$, have a weak influence on the calculation results. To demonstrate this, the calculation errors for the resonant interval and levitation force versus $\tilde{H}_b$ are depicted in Figs. 7(a) and 7(b), respectively. The calculation errors of $\tilde{H}$ are less than $\pm0.1\%$, which means the influence of $\tilde{H}_b$ on $\tilde{H}$ is negligible. The calculation errors of $\tilde{F}_{zM}$ are not beyond 25%, which seems a little larger. However, compared with the roles of $\tilde{R}_a$, $\tilde{R}_b$, and $\tilde{R}$, which affect $\tilde{F}_{zM}$ in the way of orders of magnitude, the influence of $\tilde{H}_b$ is still very small. Therefore, in the following sections, we will omit the roles of $\tilde{H}_a$ and $\tilde{H}_b$, and merely discuss the geometric parameters of $\tilde{R}_a$, $\tilde{R}_b$, and $\tilde{R}$.

IV. RESULTS AND DISCUSSIONS

A. Spherically curved reflectors

The spherically concave reflectors being studied can be divided into three categories according to their section radius, i.e., $R_b=0.737\lambda$, 0.982λ, and 1.228λ, respectively. For

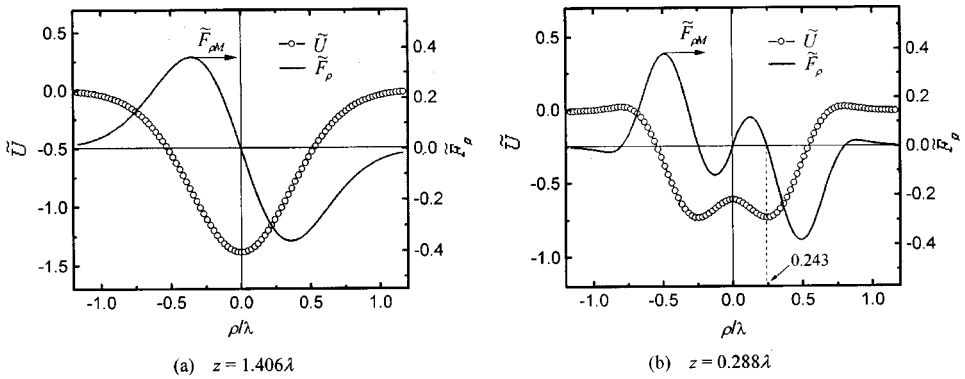

FIG. 6. The distribution of $\tilde{U}$ and $\tilde{F}_\rho$ along x axis. The figures give two different types of potential minima: (a) a minimum point and (b) a circle.

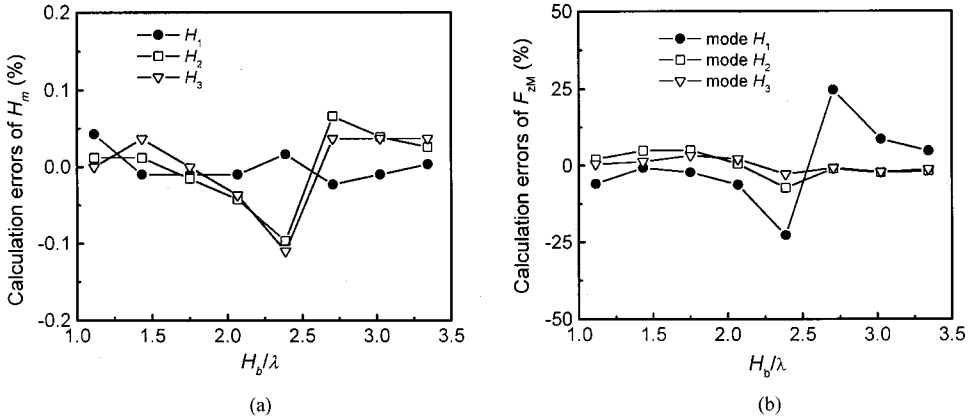

FIG. 7. Calculation errors of (a) H_m and (b) F_{zM} versus H_b/λ. The applied parameters are $\tilde{R}_a = 3.858$, $\tilde{R}_b = 6.172$, and $\tilde{D} = 1.852$.

each category of reflector, the levitation capabilities are examined as functions of the curvature radius R. The section radius of the emitter, R_a, is fixed to be 0.614λ in these calculations. Figure 8 shows the variations of $\tilde{F}_{zM}$, $\tilde{\kappa}_z$, $\tilde{F}_{\rho M}$, and $\tilde{\kappa}_\rho$ versus R for reflectors with $R_b = 0.982\lambda$, under the first resonant mode. Obviously, the laws that govern the relationships between these four quantities and R are similar. This is true for almost all the cases. Therefore, we can employ only one of the above four quantities as a representative to discuss the geometric dependence of the levitation capabilities. Here we choose the maximum levitation force $\tilde{F}_{zM}$, because it is not only the most important quantity to weigh the levitation capabilities, but also a quantity that can be easily verified by experiment.

The dependence of $\tilde{F}_{zM}$ on R with different R_b under the first three resonant modes is summarized in Fig. 9. It should be noted that, for mode H_2 and H_3, the calculation is conducted at the potential well that is closest to the reflector. The value of R starts at $R = R_b/2$, where the corresponding reflecting surface is a hemisphere cap, and ends with R becoming a very large number, where the reflecting surface approaches a planar surface. It is visible that $\tilde{F}_{zM}$ is strongly dependent upon the curvature radius of the reflector. When the reflecting surface approaches a planar surface, the values of $\tilde{F}_{zM}$ for the cases of $R_b = 0.737\lambda$, 0.982λ, and 1.228λ are of the same order of magnitude. Whereas when the reflecting surface approaches a hemisphere cap, there will be significant difference in the magnitude of $\tilde{F}_{zM}$ among the three curves. About in the region of R being within one to several times of a wavelength, each of the three curves reaches its maximum value at a certain optimum curvature radius, R_{opt}. Therefore, it is possible to enhance the levitation force by choosing an appropriate curvature radius of the reflector. The degree of enhancement by this means is different for each class of reflectors and various resonant modes, which can be measured by the ratio of $\tilde{F}_{zM}$ at the optimum curvature radius ($R = R_{\text{opt}}$) to that with a planar reflecting surface ($R = \infty$), i.e., $\tilde{F}_{zM}(R_{\text{opt}})/\tilde{F}_{zM}(R_\infty)$, as shown in Table I. It can be concluded that, the larger the section radius of a reflector is, the larger is the degree of enhancement of its levitation force by curving its reflecting surface; and that the smaller the resonant mode number is, the larger is the possibility to increase the levitation force by this means.

When the reflecting surface is very close to a hemisphere cap, the value of $\tilde{F}_{zM}$ for $R_b = 0.737\lambda$ has an abrupt rise. But with a near hemisphere cap, the reflecting surface is too deep for us to observe and manipulate the sample with sufficient convenience. In the practical design of a reflector, the surface that is close to a hemisphere cap is generally not employed.

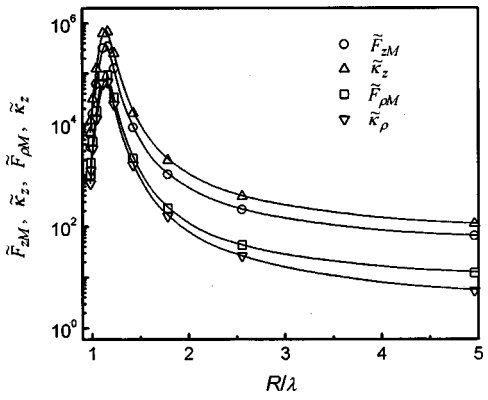

FIG. 8. $\tilde{F}_{zM}$, $\tilde{\kappa}_z$, $\tilde{F}_{\rho M}$, and $\tilde{\kappa}_\rho$ versus R/λ for reflectors with $R_b = 0.982\lambda$ under mode H_1.

B. Reflecting surface of paraboloid and hyperboloid of revolution

We also studied the reflectors with a paraboloid or hyperboliod of revolution surface. Figure 10 shows the variations of $\tilde{F}_{zM}$ as functions of depth D for these two types of reflectors as well as for spherically curved reflectors. The section radius of these reflectors is $R_b = 0.982\lambda$. The variation of D is within the region of $0 < D \leqslant R_b$. It is obvious that $\tilde{F}_{zM}$ is strongly dependent on the depth of the reflecting surface for

TABLE I. $\tilde{F}_{zM}(R_{\text{opt}})/\tilde{F}_{zM}(R_\infty)$ values for reflectors with different R_b.

R_b/λ	Mode H_1	Mode H_2	Mode H_3
1.228	38715	314.5	10.75
0.982	12928	39.54	3.765
0.737	7.129	1.761	1.240

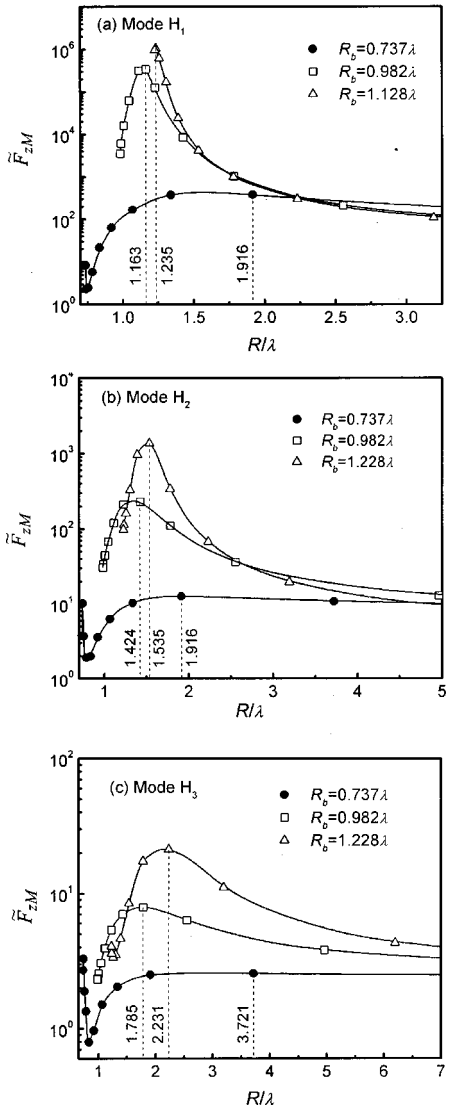

FIG. 9. Dependence of $\tilde{F}_{zM}$ on R/λ for reflectors with $R_b = 0.737\lambda$, 0.982λ, and 0.982λ under (a) mode H_1, (b) mode H_2, and (c) mode H_3.

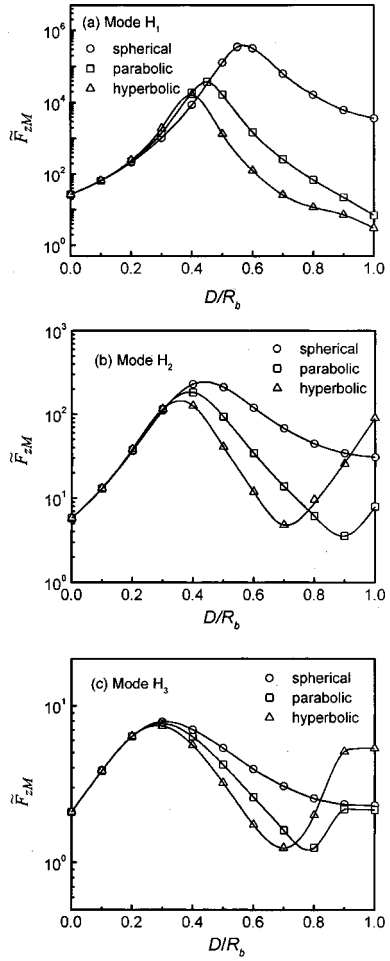

FIG. 10. Calculated $\tilde{F}_{zM}$ versus D/R_b for different reflectors under (a) mode H_1, (b) mode H_2, and (c) mode H_3.

all the three types of reflectors and all the first three resonant modes. When D approaches an infinite small value, the reflecting surfaces of all the three types of reflectors become a planar surface. Hence it is natural that in this circumstance the values of $\tilde{F}_{zM}$ for the three curves will have the same magnitude under all the three modes. With the variation of D from 0 to R_b, there always exists a maximum of $\tilde{F}_{zM}$, which means that the largest levitation force can be obtained by choosing a proper depth of the reflecting surface. This depth is denoted as the optimum depth, D_{opt}. Similarly, we can use the ratio of $\tilde{F}_{zM}$ at $D=D_{\mathrm{opt}}$ to that at $D=0$, i.e., $\tilde{F}_{zM}(D_{\mathrm{opt}})/\tilde{F}_{zM}(0)$, to weigh the degree of the levitation force enhancement. The result is shown in Table II, from which it is visible that, the smaller the resonant mode number is, the larger is the degree of enhancement. Under mode $H3$, the degrees of enhancement for the three types of reflectors are nearly the same. It can be also found that for these three types of reflectors, those with a spherically concave surface have the largest potential for levitation force enhancement by choosing appropriate depth, whereas those with a reflecting surface of a hyperboloid of revolution have the smallest potential.

Although a large depth of the reflecting surface can increase the levitation force remarkably, it may also hinder the access to the levitated sample, especially in mode H_1. In the practical design of a reflector, the convenience of observing and manipulating the sample must be taken into consideration. Thus the depth of the reflector should not be too large. Experience tells us that the value of D should be less than $\lambda/2$.

TABLE II. $\tilde{F}_{zM}(R_{\mathrm{opt}})/\tilde{F}_{zM}(0)$ values for reflectors with different reflecting surfaces.

Reflecting surface	Mode H_1	Mode H_2	Mode H_3
Spherical	12928	39.54	3.765
Parabolic	1386	31.52	3.671
Hyperbolic	598.9	21.73	3.527

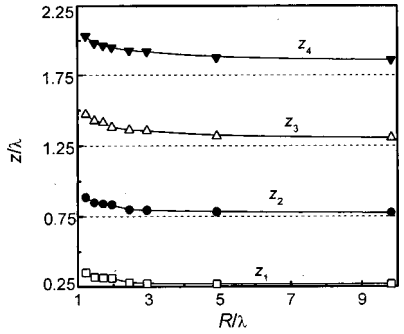

FIG. 11. The vertical positions of the sample under mode H_4 versus R/λ. Here, $R_b=0.982\lambda$.

C. Levitation positions

Generally speaking, if the single-axis acoustic levitator works at a resonant state with $H=H_m$, there will be m positions for the levitated sample under the condition of $g=0$. Figure 11 shows the vertical positions of the four potential wells under mode H_4 as a function of R. With the increasing of R, the positions of the sample are slightly lowered. It can be seen that, for a practical levitator, the positions of the sample are a little higher than those predicted by the plane standing wave analysis, which is $z=\lambda/4$, $3\lambda/4$, $5\lambda/4$, and $7\lambda/4$. Moreover, the interval between two adjacent samples is a little longer than $\lambda/2$ since H_4 is larger than four times half a wavelength.

The axial symmetry deviation of the sample closest to the reflector or emitter is often observed in experiment. This cannot find an explanation from the plane standing wave description of the acoustic field. With our model, it can be explained naturally by the space distribution of the acoustic field. Figure 12 shows the radial position of the lowest sample as a function of the reflecting surface depth D under different resonant modes. It is found that the deviation is generally within the scope of $R_b/2$, and likely to occur when the reflector has a deeper reflecting surface, a smaller section radius, and is working at a higher resonant mode.

V. COMPARISON WITH EXPERIMENT

A. Experimental method to evaluate $\tilde{F}_{zM}$

We have built up a single-axis acoustic levitator [30,32] driven by a magnetostrictive transducer. The working frequency of this transducer is 16.7 kHz, and its electric power is indicated by the input current I. With the knowledge of enhancing the levitation ability by optimizing the geometric parameters of its reflector, as stated in the previous sections, we are able to levitate samples as dense as an iridium sphere with a diameter of 4 mm, which has the largest density of 22.6 g/cm^3 in the world. For a given sample with a density ρ_s, there exists a corresponding minimum current I_m, which is necessary to have that sample levitated. The magnitude of I_m can be determined by gradually reducing the input current until the previously levitated sample falls down to the reflector. Changing the material of the samples, and repeating the above experiment, we can get a group of I_m versus ρ_s.

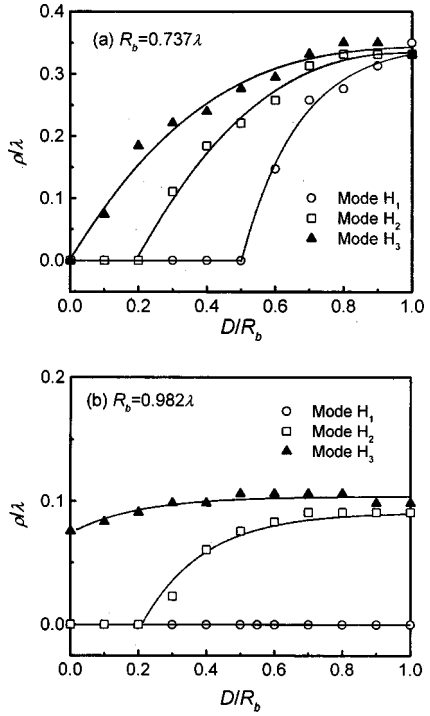

FIG. 12. The horizontal position of the sample closest to the reflector versus D/R_b under different resonant modes.

In the above experiment, the condition to determine the critical current is the balancing of the acoustic levitation force with the gravity of the sample. The gravitational force with a consideration of buoyancy has been expressed by [33]

$$F_g=\tfrac{4}{3}\pi\rho_s g R_s^3\left(1-\frac{\rho_f}{\rho_s}\right), \tag{18}$$

where ρ_s is the density of the sample and g is the gravitational acceleration. Equating F_g with F_{zM}, we can get the following relationship:

$$\rho_s=(3\rho_f k\tilde{F}_{zM}/2g)\,\nu_0^2+\rho_f. \tag{19}$$

In order to seek for relations to the experiment, the vibrating amplitude ν_0 of the emitter is assumed to be proportional to the indicating current of the transducer, then

$$\rho_s=\alpha I_m^2+\rho_f, \tag{20}$$

in which α is a coefficient proportional to $\tilde{F}_{zM}$. The value of α can be determined experimentally by a linear fitting to the $\rho_s\sim I_m^2$ relationship. We choose the value of $\tilde{F}_{zM}$ and α under a set of fixed geometric parameters as the reference values, i.e.,

$$\tilde{F}_{zM}^{(R)}=\tilde{F}_{zM}(Q^{(R)},\{X_i^{(R)}\}/\lambda) \tag{21}$$

and

$$\alpha^{(R)}=\alpha(Q^{(R)},\{X_i^{(R)}\}/\lambda). \tag{22}$$

TABLE III. List of levitated samples for $\rho_z \sim I^2$ fitting.

Material	Density (g/cm^3)	Size (mm)
Polymer	1.03	ϕ4.2
Al	2.70	ϕ4
Sn	7.28	ϕ3
Fe	7.86	ϕ4
Pb	11.34	ϕ2.8
W	18.92	ϕ3.2×2.9

Then it is easy to compare the calculation with experiment through

$$\tilde{F}_{zM}/\tilde{F}_{zM}^{(R)} = \alpha/\alpha^{(R)}. \tag{23}$$

Six different kinds of materials are levitated in the experiment for $\rho_s \sim I_m^2$ fittings, as shown in Table III. The vibrating head is fixed in the experiment with $R_a = 12.5$ mm and the samples are always levitated at the position closest to the reflector when the resonant mode number is above H_2. The geometric parameters of the reflector are divided into three groups according to R_b, namely, $R_b = 15$, 20, and 25 mm, respectively. Each group has three to four values for R (see Table IV). Some of the linear fittings to the $\rho_s \sim I_m^2$ relationship are plotted in Fig. 13, and the fitting values of α are summarized in Table V.

It should be noted that the input current is confined in a range of $0.09 \leqslant I \leqslant 0.28$ A in the experiment. Here, 0.09 A is the minimum current that can motivate the ultrasonic vibration, and a current below 0.28 A is safe for the normal work of the transducer. If the levitation force with a reflector is strong enough, the minimum currents necessary for levitating the six samples are all 0.09 A. On the other hand, if the levitation force with a reflector is weak enough, there will be only one or no sample that can be levitated below 0.28 A. In both of these two cases, the fitting values of α cannot be obtained.

B. Comparison of calculations with experiments on $\tilde{F}_{zM}$

In the following comparison of calculation with experiment, the section radius of the emitter is fixed as R_a = 12.5 mm, and the reference is set as the reflector with $R_b = 20$ and $R = 40$ mm working at mode H_2. So the dependence of $\tilde{F}_{zM}$ on the section radius and curvature radius of the reflector and on the mode number is discussed, as shown in Fig. 14. It can been seen that

TABLE IV. List of reflector parameters.

Reflectors	R_b (mm)	R (mm)
No. 1	15	17
No. 2	15	19.5
No. 3	15	25
No. 4	20	25
No. 5	20	29
No. 6	20	36
No. 7	20	40
No. 8	25	32
No. 9	25	39
No. 10	25	55

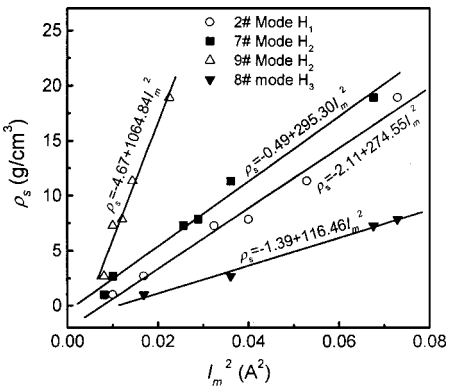

FIG. 13. Linear fittings to $\rho_s \sim I_m^2$ for some reflectors under various resonant modes.

(1) For the same reflector, the levitation force decreases with the increasing of the mode number.

(2) The calculation agrees well with the experiment on the $\tilde{F}_{zM}/\tilde{F}_{zM}^{(R)}$-$R_b/\lambda$-$R/\lambda$-mode dependence, especially when $R_b = 0.737\lambda$ and 0.982λ. In the case of $R_b = 1.228\lambda$, the variation tendency of $\tilde{F}_{zM}/\tilde{F}_{zM}^{(R)}$ for experiment and calculation are also in agreement.

(3) In Figs. 14(b) and 14(c), the intensively increasing tendency of $\tilde{F}_{zM}/\tilde{F}_{zM}^{(R)}$ with decreasing of R/λ for mode H_1 is not evidently demonstrated by experimental data. The reason lies in two aspects. On one hand, with larger section radius and near optimum curvature radius, the levitation force is strong enough, so that the critical indicating currents to levitate the six samples are all 0.09 A. In this case, the experimental date for $\tilde{F}_{zM}/\tilde{F}_{zM}^{(R)}$ is unavailable. On the other hand, it is surprising of the calculation that the increasing tendency of $\tilde{F}_{zM}/\tilde{F}_{zM}^{(R)}$ with decreasing of R becomes so steep, when R is approaching the optimum value. Since the calculation is based on linear equations of the acoustic field,

TABLE V. Fitting value of α.

	α		
Reflectors	Mode H_1	Mode H_2	Mode H_3
No. 1	55		
No. 2	274.55		
No. 3	1341.52	41.8	
No. 4		587.80	
No. 5		753.02	39.53
No. 6	3987.89	404.79	49.76
No. 7	1202.70	295.30	41.28
No. 8		1894.25	126.46
No. 9	3987.89	1064.84	370.85
No. 10	336.57	222.18	107.89

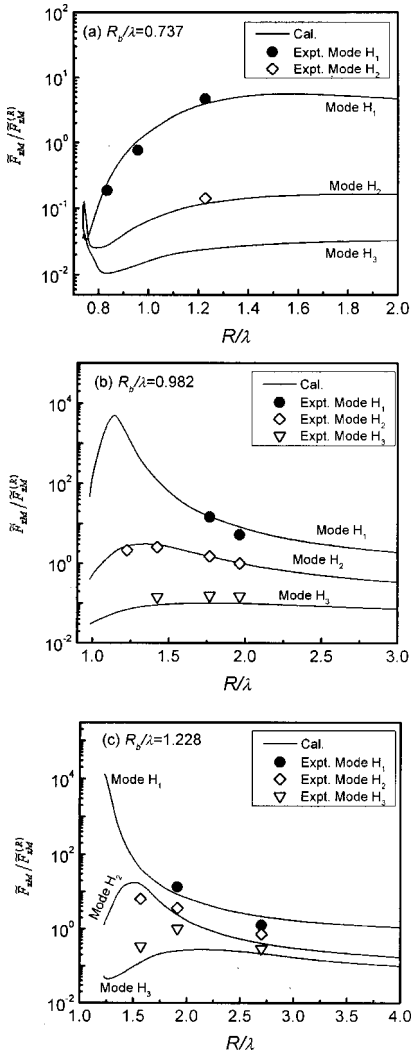

FIG. 14. Comparison of calculation with experiment on dependence of $\tilde{F}_{zM}/\tilde{F}_{zM}^{(R)}$ as a function of R/λ under the first three modes with (a) $R_b/\lambda = 0.737$, (b) $R_b/\lambda = 0.982$, and (c) $R_b/\lambda = 1.228$.

no absorption or attenuation is taken into consideration, whereas the nonlinear effects and absorption cannot be neglected when the acoustic field becomes ultraintense. Therefore, it is guessed that the actual tendency is not so steep.

(4) Both the calculation and experiment suggest that, to obtain the best levitation ability, the single-axis acoustic levitator should be operated under mode 1 using a reflector with a large section radius R_b and an appropriate curvature radius R.

VI. CONCLUSIONS

Single-axis acoustic levitation capabilities are strongly dependent on the geometric parameters of the levitator. To study this geometric dependence systematically, a two-cylinder model incorporating boundary element method simulation is developed. According to this model, the levitation force and stability are functions of the emitter section radius R_a, the reflector section radius R_b, the curvature radius R (or depth D), and the resonant mode number H_m ($m = 1,2,3,...$). This model proves to be successful in predicting the resonant modes of acoustic field and explaining the deviation of the samples near the reflector and emitter.

On the basis of this model, the reflecting surfaces of a spherical cap, a paraboloid of revolution, and a hyperboloid of revolution with various section radii R_b and different curvature radii R or depths D are systematically investigated. The calculations show that it is possible to enhance the levitation force of a levitator by optimizing the curvature radius or depth of its reflector, and that the smaller the resonant mode, the larger the degree of enhancement is. Among the three shapes of reflecting surfaces, the largest degree of enhancement in levitation force can be obtained for spherical reflecting surfaces by this means. As to the reflectors with spherically concave surfaces, the larger the section radius is, the larger is the possibility to increase its levitation force by choosing an appropriate curvature radius. It is also revealed that the axial symmetry deviation of the sample closest to the reflector is likely to occur when the reflector has a deeper reflecting surface, a smaller section radius, and is working at a higher resonant mode.

We also developed an experimental method to verify the dependence of levitation force on the geometric parameters of the reflector, in which remarkable enhancement in levitation force is achieved so as to levitate an iridium sphere that has the largest density of $\rho_s = 22.6$ g/cm^3. The experimental data and the calculated results are in good agreement, which indicates that better levitation capabilities can be obtained by working under mode H_1 and applying a spherically concave reflector with a large section radius R_b and an appropriate curvature radius R.

ACKNOWLEDGMENTS

This work is supported by the National Natural Science Foundation of China under Grants Nos. 50221101, 50101010, and 59901009, and the Doctorate Foundation of Northwestern Polytechnical University.

[1] E. H. Brandt, Nature (London) **413**, 474 (2001).
[2] J. K. R. Weber, J. J. Felten, B. Cho, and P. C. Nordine, Nature (London) **393**, 769 (1998).
[3] D. M. Herlach, R. F. Cochrane, I. Egry, H. J. Fecht, and A. L. Greer, Int. Mater. Rev. **38**, 273 (1993).
[4] R. Willnecker, D. M. Herlach, and B. Feuerbacher, Phys. Rev. Lett. **62**, 2707 (1989).
[5] I. Egry, and S. Sauerland, Mater. Sci. Eng., A **178**, 73 (1994).
[6] S. Ansell *et al.*, Phys. Rev. Lett. **78**, 464 (1997).
[7] E. H. Trinh and K. Ohsaka, Int. J. Thermophys. **16**, 545 (1995).
[8] E. H. Trinh, J. Acoust. Soc. Am. **95**, 567 (1994).
[9] R. G. Holt and E. H. Trinh, Phys. Rev. Lett. **77**, 1274 (1996).
[10] T. G. Wang, E. H. Trinh, A. P. Croonquist, and D. D. Elleman,

Phys. Rev. Lett. **56**, 452 (1986).
[11] E. H. Brandt, Science **243**, 349 (1989).
[12] S. Bauerecker and B. Neidhart, J. Chem. Phys. **109**, 3709 (1998).
[13] T. Volkman, G. Wilder, R. Willnecker, and D. M. Herlach, J. Appl. Phys. **83**, 3028 (1998).
[14] W. K. Rhim, K. Ohsaka, and P. F. Paradis, Rev. Sci. Instrum. **70**, 2796 (1999).
[15] K. Nagashio, K. Kuribayashi, and Y. Takamura, Acta Mater. **48**, 3049 (2000).
[16] M. V. Berry and A. K. Geim, Eur. J. Phys. **18**, 307 (1997).
[17] A. K. Geim, M. D. Simon, M. I. Boamfa, and L. Q. Heflinger, Nature (London) **400**, 323 (1999).
[18] M. Barmatz and P. Collas, J. Acoust. Soc. Am. **77**, 928 (1985).
[19] L. V. King, Proc. R. Soc. London, Ser. A **147**, 212 (1934).
[20] M. Barmatz, *Proceedings of the 1984 Ultrasonics Symposium* (Institute of Electrical and Electronics Engineers, New York, 1984), p. 436
[21] E. Lierke, R. Grossbach, K. Floegel, and P. Clancy, *Proceedings of the 1983 Ultrasonics Symposium* (Institute of Electrical and Electronics Engineers, New York, 1983), p. 1129.
[22] P. M. Gammel, A. P. Croonquist, and T. G. Wang, J. Acoust. Soc. Am. **83**, 496 (1988).
[23] E. H. Trinh, Rev. Sci. Instrum. **56**, 2059 (1985).
[24] J. Magill, F. Capone, R. Beukers, P. Werner, and R. W. Ohse, High Temp.-High Press. **19**, 461 (1987).
[25] M. C. Lee and I. Feng, Rev. Sci. Instrum. **53**, 854 (1982).
[26] W. A. Oran, L. H. Berge, and H. W. Parker, Rev. Sci. Instrum. **51**, 625 (1980).
[27] K. Ohsaka and E. H. Trinh, J. Cryst. Growth **96**, 973 (1989).
[28] K. Ohsaka, E. H. Trinh, and M. E. Glicksman, J. Cryst. Growth **106**, 191 (1990).
[29] Y. Bayazitoglu and G. Hell, J. Thermophys. Heat Transfer **16**, 545 (1996).
[30] W. J. Xie and B. Wei, Chin. Phys. Lett. **18**, 68 (2001).
[31] L. P. Gor'kov, Dokl. Akad. Nauk SSSR **140**, 88 (1961) [Sov. Phys. Dokl. **6**, 773 (1962)].
[32] W. J. Xie and B. Wei, Appl. Phys. Lett. **79**, 881 (2001).
[33] P. Collas, M. Barmatz, and C. Shipley, J. Acoust. Soc. Am. **86**, 777 (1989).